Proceedings of the 11th World Congress on Civil, Structural, and Environmental Engineering (CSEE 2026)
Paris, France - April, 2026
Paper No. ICSECT 121
DOI: 10.11159/icsect26.121

Seismic Behavior of Post-Tensioned Reinforced Concrete Beam-to-Column Joints

Erturk Tuncer[1], Can Karageyik[2], Erdem Canbay[2], Norgen Muka[2], Baris Binici[2]
[1]Department of Civil Engineering, TED University
Cankaya, Ankara 06420, Turkey
erturk.tuncer@tedu.edu.tr; can.karageyik@metu.edu.tr; ecanbay@metu.edu.tr; muka.norgen@metu.edu.tr; binici@metu.edu.tr
[2]Department of Civil Engineering, Middle East Technical University
Cankaya, Ankara 06800, Turkey

Abstract - Post-tensioned buildings provide notable advantages including reduced frame weight, lower seismic demands, and enhanced resistance to applied loading. While numerous research has focused on post-tensioned precast beam-to-column joints, limited attention has been given to the seismic behavior of cast-in-place reinforced concrete connections incorporating post-tensioning. This study addresses this gap by experimentally examining the seismic performance of representative sub-assemblages. The primary test parameters were defined as the mild steel ratio, load-balancing ratio, and connection configuration. The experimental program was evaluated through comparisons of base shear–lateral displacement, moment–curvature, crack width development, energy dissipation, equivalent viscous damping ratio, and stiffness degradation of the specimens. Accordingly, it was found that post-tensioned beam-to-column joints can provide satisfactory structural performance and adequate ductility when the amounts of mild steel and prestressing steel are properly optimized. Moreover, post-tensioned specimens exhibited more uniform crack patterns and smaller crack widths than conventional reinforced concrete specimens due to the self-centering capability of tendons.

***Keywords*:** Post-tensioning, seismic performance, beam-to-column connection, reinforced concrete

1. Introduction

Post-tensioning technology utilizing high-strength concrete and steel is particularly well-suited for long-span beams in moment-resisting frame buildings. As spans increase, reinforced concrete (RC) design is often governed by serviceability requirements, even when strength and ductility targets are satisfied. In such cases, post-tensioning provides an economically and architecturally viable solution [1,2]. Its advantages include thinner slabs, reduced floor-to-floor heights, smaller deflections, and narrower crack widths under service loads compared with conventional RC frames. At design stage, both immediate and time-dependent prestress losses are calculated for gravity load conditions. Stresses in the concrete section are verified at transfer and under service loads to remain within permissible limits defined by design codes (e.g., TS3233 [3], Eurocode 2 [4], ACI 318 [5]). Cross-sectional dimensions, tendon profiles, and mild steel reinforcement are selected to satisfy ultimate limit state requirements, thereby ensuring compliance with gravity load design criteria. In seismic design, the response spectrum method described in TBEC [6], Eurocode 8 [7], ASCE/SEI 7 [8]) is used to estimate lateral forces by incorporating coefficients such as the response modification factor and overstrength factor. A considerable body of experimental and numerical research has investigated post-tensioned beam-to-column joints [9–11]. Most studies examined hybrid systems combining prestressing strands with mild steel, where the latter provides energy dissipation and the former ensures self-centering. These connections generally demonstrated adequate lateral strength, stiffness, and residual deformation control compared with monolithic RC joints, but their energy dissipation capacity remained lower. To address this limitation, recent studies have proposed external energy dissipating devices—including friction dampers, fuse-type dissipaters, lead-extrusion dampers, and steel angles—to enhance seismic performance [12–15]. Experimental investigations by Kim et al. [16] evaluated the influence of grout type, slab presence, and tendon length on cyclic response. Specimens with slabs exhibited shear failures, whereas those without slabs primarily failed by concrete crushing. Similarly, Hwang et al. [17] explored the effect of prestress level, reporting that higher prestressing forces triggered early joint crushing, thereby emphasizing the need for strong transverse confinement. Numerical approaches have also been widely implemented: Paudel

et al. [18] analyzed stress trajectories and damage patterns in precast joints; Zhipeng et al. [19] developed a nonlinear finite element model capable of simulating plastic hinge formation; and Li et al. [20] conducted parametric analyses on mild steel ratios and bonded strand lengths to investigate shear resistance. Furthermore, Khodaei et al. [21] and Maddah et al. [22] demonstrated that integrating post-tensioning rods with L-shaped steel angles enlarged joint cores, enhanced load-bearing capacity, reduced pinching effects caused by bar slip, and promoted flexural plastic hinge mechanisms. Although previous studies have substantially advanced the understanding of beam-to-column connections in prestressed precast systems, limited experimental research has addressed post-tensioned cast-in-place reinforced concrete connections. To bridge this gap, five specimens were designed and tested under reverse cyclic loading with key parameters including the mild steel ratio, load-balancing ratio, and joint geometry. The investigation focused on lateral load–displacement response, moment–curvature relationship, crack width development, energy dissipation capacity, equivalent viscous damping, stiffness degradation, and displacement ductility.

2. Laboratory Tests

The typical floor plan of a four-story prototype building is shown in Fig. 1a. The total center-to-center spans are 50.7 m in the longitudinal direction and 24 m in the transverse direction. Each story has a height of 3.2 m with a 20 cm-thick slab. Columns and beams were designed with cross-sectional dimensions of 90 × 90 cm and 80 × 80 cm, respectively. Exterior and interior beam-to-column joint types are indicated in Fig. 1b. Post-tensioning design followed ACI 318 [5], while seismic design adhered to TBEC [6]. In the experimental program, 1:2 scale specimens were constructed due to laboratory capacity limitations (Figs. 1c-d). Typical reinforcement details for all structural elements are also shown in Fig. 2. In the same figure, parabolically varied tendon layouts for exterior and interior specimens are depicted. An effective prestress (f_{pe}) of approximately 1100 MPa, corresponding to 60% of the ultimate strength (f_{pu}), was applied to all post-tensioned specimens. In total, five specimens were tested. Table 1 presents the properties of the test specimens. The main test variables were the mild steel ratio, load-balancing ratio, and specimen geometry. Specifically, SP_01 and SP_02 were tested to assess the effect of mild steel ratio; SP_01 and SP_03 were compared to investigate the influence of load-balancing ratio; and SP_02 and SP_04 were examined to study the effect of geometry (interior vs. exterior joints). A reference specimen, SP_05, reinforced solely with mild steel, was also included. The experimental setups illustrated in Figs. 3a–b, were constructed using support elements, loading equipment, and measurement instruments. The boundary conditions were established according to the inflection points of 1:2 scaled test frames: the beam was supported by a roller at its free end to permit horizontal displacement, while vertical restraint was provided through a pinned support at the column base. Accordingly, the roller was positioned 1.55 m from the column face, defining the beam shear span, and the column hinge and horizontal actuator were placed 0.8 m from the column ends, corresponding to the column shear span. After installation, prestressing was introduced through a horizontal hydraulic jack with a 100-ton capacity. Axial force was applied incrementally to the column using two vertical jacks (each 100 tons) and was maintained at 85 tons corresponding to ~10% of the column capacity throughout the tests. Lateral loading was then imposed by a 50-ton hydraulic actuator following the quasi-static displacement history of FEMA 461 [23].

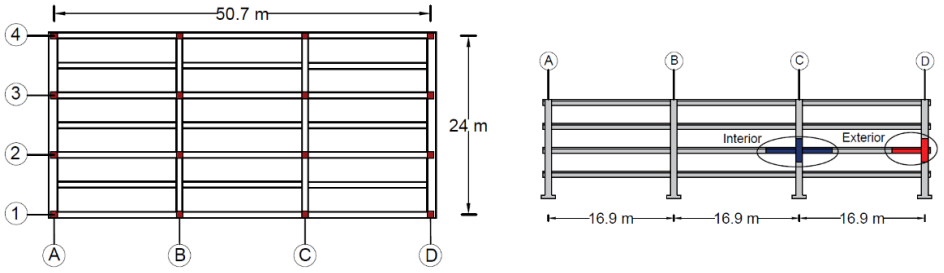

(a) Floor plan (b) Joint types

Fig. 1: Prototype building and test specimen geometry

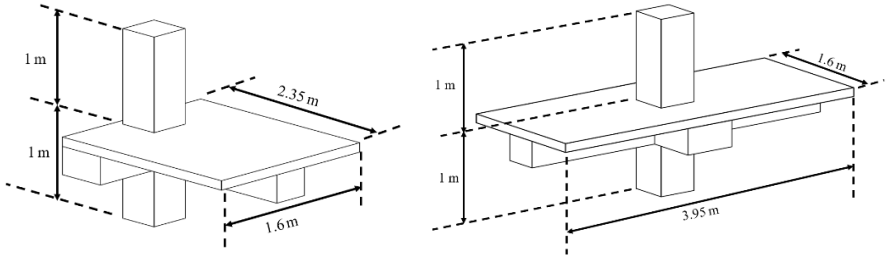

(c) Exterior joint dimensions (d) Interior joint dimensions

Fig. 1 (cont'd)

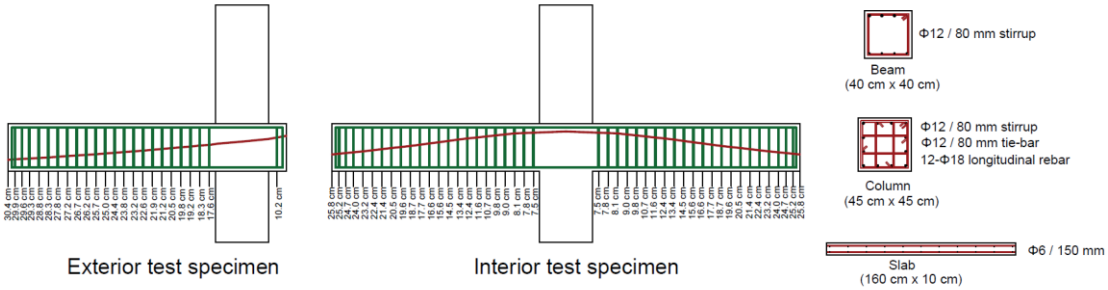

Fig. 2: Reinforcement details

Table 1**:** Properties of test specimens

Specimen	f_c' (MPa)	f_y (MPa)	f_u (MPa)	f_{pu} (MPa)	ρ	A_{ps} (mm^2)	Load-balancing ratio (%)
SP_01	44	557	692	1852	0.003	2×150	50
SP_02	40	555	679	1849	0.004	2×150	50
SP_03	47	557	692	1864	0.003	3×150	75
SP_04	45	555	679	1860	0.004	2×150	50
SP_05	49	553	673	-	0.010	-	-

(*) f_c': Compressive strength of concrete, f_y: yield strength of mild steel, f_u: ultimate strength of mild steel, ρ: mild steel ratio, A_{ps}: tendon area.

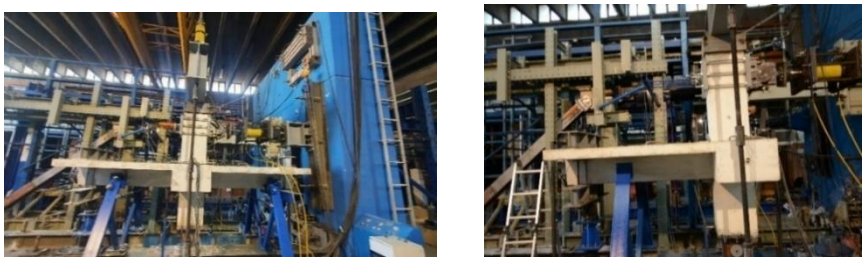

(a) Interior test specimen (b) Exterior test specimen

Fig. 3: Test setup

3. Test Results

The experimentally derived moment–curvature relationships are presented in Fig. 4, together with analytical predictions obtained through fiber-based sectional analyses. These analyses incorporated the confined concrete model proposed by Mander et al. [24] and assumed a bilinear stress–strain response for both the reinforcing steel and the post-tensioning tendons.

The comparison between experimental data and analytical estimations highlights the reliability of the adopted modeling approach. The global seismic response of the specimens is illustrated in Fig. 5, which displays the hysteretic base shear–lateral displacement behavior of the beams alongside the principal damage states observed during testing. Fig. 6 reports the maximum and residual crack widths recorded at each drift ratio, providing a quantitative measure of cracking progression. The curves of cumulative dissipated energy, equivalent viscous damping ratio, and normalized stiffness degradation are presented in Fig. 7. Test results are summarized in Table 2 (positive sign: push direction, negative sign: pull direction). Further details can be found in the study conducted by Tuncer et al. [25].

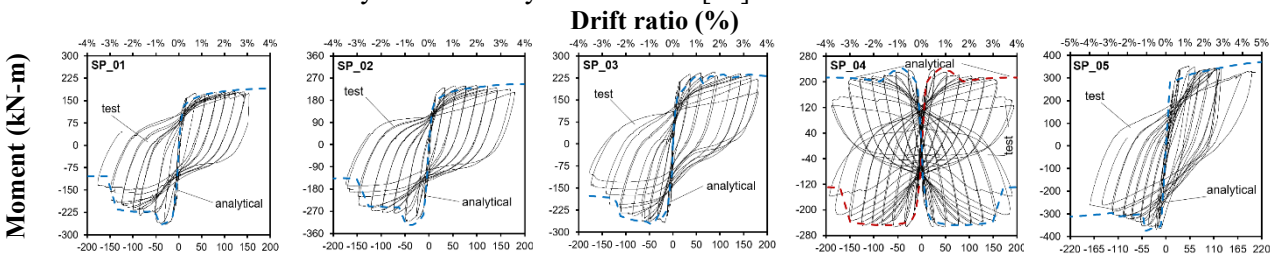

Fig. 4: Moment-curvature relationship

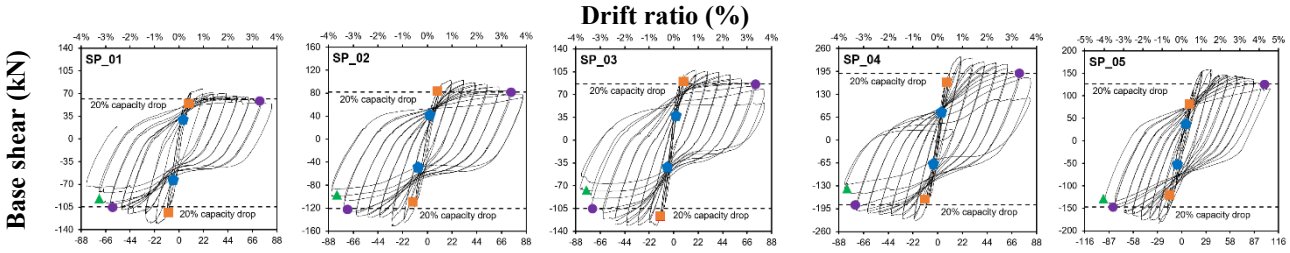

Fig. 5: Base shear-lateral displacement relationship

(*) Square: First cracking, Triangle: Yielding, Circle: Concrete crushing, Diamond: Longitudinal bar buckling

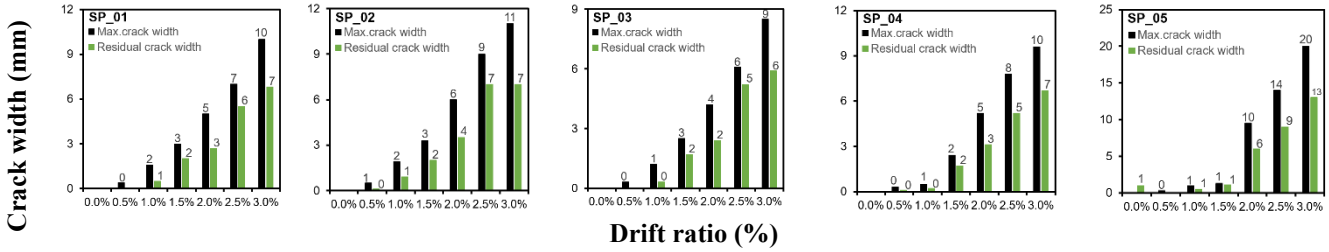

Fig. 6: Maximum and residual crack width measurements

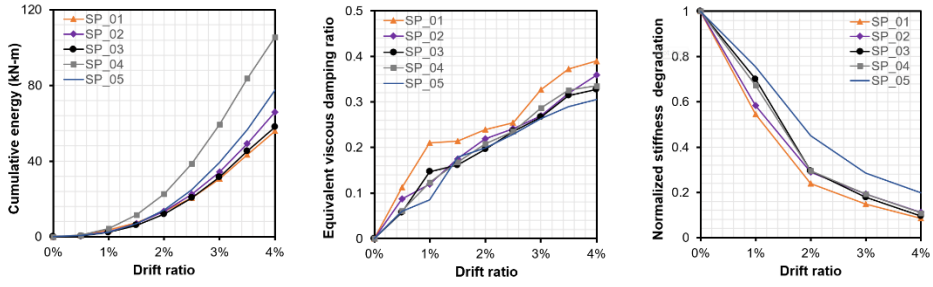

(a) (b) (c)

Fig. 7: Cumulative energy (a), equivalent viscous damping ratio (b), normalized stiffness degradation (c)

Table 2**:** Summary of test results

Specimen	K_i^+ (kN/m)	Δ_y^+ (mm)	Δ_u^+ (mm)	ϕ_y^+ (rad/km)	ϕ_u^+ (rad/km)	μ_Δ^+	μ_ϕ^+	V_y^+ (kN)	V_{ult}^+ (kN)	M_{max}^+ (kN-m)
SP_01	8992.6	6.75	68.21	9.83	143.98	10.1	14.6	60.7	77.2	181.2
SP_02	10492.9	7.71	73.22	9.91	121.40	9.5	12.2	80.9	102.2	240.0
SP_03	14060.0	6.33	71.25	10.29	178.56	11.3	17.4	89.0	107.7	246.2
SP_04	22403.1	7.74	72.52	10.56	177.43	9.4	16.8	173.4	236.3	237.6
SP_05	10140.1	7.85	96.50	9.81	206.67	12.3	21.1	79.6	158.8	352.6
Specimen	K_i^- (kN/m)	Δ_y^- (mm)	Δ_u^- (mm)	ϕ_y^- (rad/km)	ϕ_u^- (rad/km)	μ_Δ^-	μ_ϕ^-	V_y^- (kN)	V_{ult}^- (kN)	M_{max}^- (kN-m)
SP_01	11228.1	9.69	54.38	10.47	95.52	5.6	9.1	108.8	130.7	266.1
SP_02	10577.3	10.74	69.34	10.64	119.95	6.5	11.3	113.6	151.1	311.7
SP_03	10535.2	11.21	70.70	11.10	111.82	6.3	10.1	118.1	131.3	268.7
SP_04	20422.4	8.76	72.47	10.29	170.96	8.3	16.6	178.9	239.7	254.1
SP_05	12482.0	9.71	81.96	9.26	116.13	8.4	12.5	121.2	183.4	371.8

(*) Δ_y: Yield displacement, Δ_u: ultimate displacement, ϕ_y: yield curvature, ϕ_u: ultimate curvature, V_y: yield lateral load, V_{ult}: ultimate lateral load, M_{max}: maximum moment at the joint, K_i: initial stiffness (V_y/Δ_y), μ_Δ: displacement ductility (Δ_u/Δ_y), μ_ϕ: curvature ductility (ϕ_u/ϕ_y),

4. Evaluation of Test Results

4.1 Moment-curvature

Fig. 4 illustrates that abrupt strength losses occurred in the pull direction as a result of slab reinforcement and prestressing strand fracture. Among all tested beams, SP_05 reached the highest flexural strength in both loading directions (Table 2), emphasizing that increasing the longitudinal reinforcement ratio is more effective for improving moment capacity than supplementing a lower amount of mild steel with post-tensioning. The role of longitudinal reinforcement was first examined by comparing specimens SP_01 and SP_02. The latter attained approximately 33% greater moment capacity in positive loading and about 17% greater in negative loading, where the tendon force contributed significantly at the joint. This difference reflects the influence of partial prestressing, which enhances capacity but diminishes the share of resistance carried by mild steel. The pull-to-push moment ratios of about 1.5 for SP_01 and 1.3 for SP_02 indicate that the contribution of prestressing is more pronounced when the mild steel ratio is lower. A second comparison was drawn between SP_01 and SP_03 to assess the effect of load-balancing. While the push-to-pull moment ratio was roughly 1.5 for SP_01, it decreased to about 1.1 for SP_03 (Table 2). This suggests that structural performance improves as the mild-to-tendon steel ratio increases, underscoring the governing role of reinforcement distribution rather than load-balancing alone. Exterior versus interior behavior was assessed by comparing SP_02 and SP_04. Push-direction capacities were almost identical, however, SP_02 developed nearly 25% higher pull capacity (Table 2). This discrepancy is attributable to boundary conditions: the cantilever configuration of SP_02 imposed higher demands at the exterior support, whereas the symmetric tendon layout and supports of SP_04 led to a more uniform internal force distribution. Curvature ductility provided further insight into deformation capacity. All post-tensioned beams experienced lower μ_ϕ values in the pull direction due to the brittle rupture of prestressing steel. As summarized in Table 2, curvature ductility declined by about 10% in SP_02 and 40% in SP_01, highlighting the essential contribution of longitudinal reinforcement in sustaining ductility. Although an increase in load-balancing ratio (SP_01 vs. SP_03) did not significantly mitigate this loss—both showing about 40% reduction—higher reinforcement ratios were effective in preserving ductile behavior. SP_04, owing to its symmetric geometry and supports, displayed almost identical ductility in both loading directions. By contrast, SP_05 exhibited a pull-to-push ductility ratio of about 0.6, which is attributed to premature concrete crushing in the pull direction (Table 2).

4.2 Base shear-lateral displacement

The comparative evaluation of moment-curvature behavior can be extended to examine base shear–lateral displacement responses. In this context, ultimate lateral loads were assessed analogously to the maximum moments discussed previously (Fig. 5). The subsequent discussion focuses on the effect of post-tensioning on displacement ductility (μ_{Δ}) in the pull direction (Table 2). Increasing the longitudinal reinforcement ratio led to a more ductile response (SP_01 vs. SP_02). As the proportion of non-prestressed steel increased, the influence of post-tensioning diminished (i.e., a lower partial prestressing ratio), and the behavior of the member became largely governed by the ductility of mild steel. Accordingly, SP_02 exhibited approximately 1.15 times higher displacement ductility than SP_01. A higher load-balancing ratio slightly enhanced ductility (SP_01 vs. SP_03), reflecting the modest contribution of additional tensile force. Comparing exterior and interior beams (SP_02 vs. SP_04) revealed that the interior specimen achieved roughly 30% greater ductility, attributable to the symmetrically positioned roller supports, which facilitated more uniform deformation. Among all specimens, SP_05, which lacked post-tensioning, demonstrated the highest displacement ductility, highlighting the primary role of mild steel in controlling deformation capacity. In the pull direction, flexural cracking initiated at higher drift ratios due to post-tensioning, thereby reducing residual deformations and mitigating seismic vulnerability. Post-tensioned beams also reached peak loads earlier in this direction, as prestressing accelerated load development. Reinforcing steel yielded at higher drift ratios, whereas concrete crushing occurred at lower drifts. This behavior can be attributed to the combined action of mild and prestressing steel, which delays tension steel yielding through fiber-to-fiber and material-to-material stress redistribution. However, post-tensioning constrains overall deformation capacity and induces brittle behavior, leading to earlier attainment of ultimate concrete strains and the onset of cover spalling and crushing.

4.3 Crack width

Fig. 6 demonstrates that damage in the test specimens became increasingly pronounced as the loading protocol advanced. In post-tensioned beams, both maximum and residual crack widths increased with a higher longitudinal reinforcement ratio (SP_01 vs. SP_02). In contrast, SP_03 exhibited narrower cracks than SP_01, which can be attributed to its higher load-balancing ratio. Theoretically, an elevated load-balancing ratio generates additional compressive force, mitigating tensile stresses induced by vertical loads. Consequently, the lower tensile stresses in SP_03 contributed to more effective crack control, a trend confirmed by experimental observations. Additionally, SP_04 displayed smaller crack widths compared to SP_02. This behavior is linked to the symmetric boundary conditions as discussed previously. During early loading stages, residual cracks were not seen in post-tensioned specimens, whereas the conventional beam exhibited visible cracking. This observation highlights the self-centering capability of post-tensioned systems, which substantially limits residual deformations and excessive deflections compared to conventional reinforced concrete beams.

4.4 Cumulative dissipated energy, equivalent viscous damping ratio, normalized stiffness degradation

Fig. 7a shows that SP_01 and SP_03 exhibited nearly identical cumulative energy paths, reflecting the fact that both specimens contained the same amount of mild steel despite differences in tendon areas. This indicates that variations in prestressing steel had a limited influence on overall energy dissipation. At a 4% drift ratio, SP_02 dissipated approximately 15% more cumulative energy than SP_01, consistent with the pull-direction ductility levels reported in Table 2. This behavior can be attributed to the elastoplastic response and ductile nature of the mild steel. SP_05, with no post-tensioning, showed the highest cumulative energy among the exterior beams, dissipating roughly 1.2 times more energy than SP_02, further highlighting the primary role of longitudinal reinforcement in energy dissipation. SP_04 dissipated approximately 1.6 times more energy than SP_02 at 4% drift, likely due to the double-flange effect which enhanced load distribution, energy dissipation, and overall seismic performance. Analysis of equivalent viscous damping ratios (Fig. 7b) revealed similar trends for all specimens except SP_01 up to 3% drift corresponding to the onset of concrete cover spalling. At 4% drift, SP_01 exhibited the highest damping ratio (~0.4), likely resulting from earlier

concrete crushing, which produced a narrower hysteresis loop, lower strain energy-to-total energy ratio, and reduced displacement ductility. In contrast, SP_05 demonstrated the lowest equivalent viscous damping (~0.3) at the same drift, consistent with delayed concrete crushing and the highest ductile response among the specimens. Fig. 7c illustrates that normalized stiffness degradation at the beam-to-column joints consistently increased with drift level. The most rapid stiffness deterioration occurred during the initial loading stages, driven by the formation of flexural cracks. After the tension steel yielded, the rate of stiffness loss decreased, indicating a more gradual degradation. Specimens SP_01 and SP_02 displayed similar degradation trends, however, the higher longitudinal reinforcement in SP_02 resulted in slightly reduced stiffness loss. At 1% drift, SP_01 experienced nearly 1.5 times greater stiffness reduction than SP_03, reflecting the influence of tendon area and load-balancing ratio. This suggests that prestressing steel, due to its high tensile strength, enhances member stiffness, particularly when tendon area and load-balancing ratios are increased, thereby mitigating early capacity loss. Comparison between SP_02 and SP_04 indicates that SP_04 exhibited approximately 15% higher normalized stiffness at the initial loading stage (~1% drift), meaning the interior beam experienced less stiffness reduction. This improvement is attributable to the symmetrical support configuration, which facilitated uniform load transfer and reduced abrupt capacity changes. By the end of testing, all post-tensioned beams converged to nearly identical normalized stiffness ratios. SP_05, in contrast, exhibited the smallest overall stiffness reduction, indicating that stiffness preservation was largely governed by the higher proportion of longitudinal reinforcement rather than the combination of prestressing steel with limited mild steel. This behavior may also reflect superior bonding between conventional longitudinal bars and concrete compared to the bond between prestressing steel and surrounding concrete.

5. Conclusion

This study investigated the ductility of four post-tensioned reinforced concrete (RC) beams through experimental testing and numerical modeling, focusing on the effects of longitudinal reinforcement ratio, load-balancing ratio, and specimen geometry. Within the scope of the tests performed, the following conclusions were drawn:

- A sufficient amount of reinforcing steel is essential to complement prestressing steel and enhance ductile behavior in seismic applications.
- When other parameters were held constant, the influence of load-balancing ratio on displacement ductility was found to be limited.
- Post-tensioning improved self-centering capacity, which contributed to lower residual crack widths and delayed stiffness degradation, particularly during the early loading stages.
- Section analysis provided moment–curvature responses that showed good agreement with experimental measurements.

Acknowledgements

The authors would like to thank the Scientific and Technological Research Council of Turkey (TUBITAK). This work was supported by the Scientific and Technological Research Council of Turkey (TUBITAK) under grant number 119M973.

References

[1] R. I. Gilbert, N. C. Mickleborough, G. Ranzi, *Design of prestressed concrete to Eurocode 2*. CRC Press, 2017.
[2] B. O. Aalami, *Post-tensioning in building construction*. CRC Press, 2023.
[3] Turkish Standards. *Building code requirements for prestressed concrete* (TS3233), 1979.
[4] European Standard. *Eurocode 2: Design of concrete structures - Part 1-1: General rules and rules for buildings* (EN 1992-1-1), 2004.
[5] American Concrete Institute. *Building code requirements for structural concrete* (ACI 318), 2019.
[6] Turkish Standards. *Turkey building earthquake code* (TBEC), 2018.
[7] European Standard. *Eurocode 2: Design of structures for earthquake resistance - Part 1: General rules, seismic actions and rules for buildings* (EN 1998-1), 2004.

[8] American Society of Civil Engineers. *Minimum design loads and associated criteria for buildings and other structures* (ASCE/SEI 7), 2022.
[9] M. J. N. Priestley, J. R. Tao, "Seismic response of precast prestressed concrete frames with partially debonded tendons," *PCI Journal*, *38*(1). https://doi.org/10.15554/pcij.01011993.58.69, 1993.
[10] M. J. N. Priestley, G. A. MacRae, "Seismic tests of precast beam-to-column joint subassemblages with unbonded tendons," *PCI Journal*, *41*(1). https://doi.org/10.15554/pcij.01011996.64.81, 1996.
[11] J. Stanton, W. C. Stone, G. S. Cheok, "A hybrid reinforced precast frame for seismic regions," *PCI Journal*, *42*(2). https://doi.org/10.15554/pcij.03011997.20.23, 1997.
[12] C. L. Wang, Y. Liu, X. Zheng, J. Wu, "Experimental investigation of a precast concrete connection with all-steel bamboo-shaped energy dissipaters," *Engineering Structures*, *178*. https://doi.org/10.1016/j.engstruct.2018.10.046, 2019.
[13] B. G. Morgen, Y. C. Kurama, "Seismic response evaluation of posttensioned precast concrete frames with friction dampers," *Journal of Structural Engineering*, *134(1)* https://doi.org/10.1061/(ASCE)0733-9445(2008)134:1(132), 2008.
[14] L. L. Song, T. Guo, C. Chen, "Experimental and numerical study of a self-centering prestressed concrete moment resisting frame connection with bolted web friction devices," *Earthquake Engineering and Structural Dynamics*, *43*(4). https://doi.org/10.1002/eqe.2358, 2014.
[15] T. Guo, L. L. Song, R. Sause, C. Chen, "Retracted: Self-centering prestressed concrete beam-column connections with web friction devices," *Journal of Structural Engineering*, *139(4)* https://doi.org/10.1061/(ASCE)ST.1943-541X.0000801, 2012.
[16] J. H. Kim, S.H. Choi, J.H. Hwang, H. Jeong, S.H. Han, K.S. Kim, "Experimental study on lateral behavior of post-tensioned precast beam-column joints," *Structures*, *33*. https://doi.org/10.1016/j.istruc.2021.04.095, 2021.
[17] J. H. Hwang, K.S. Kim, S.H. Choi, O.S. Kwon, D.H. Lee, "Seismic behaviour of post-tensioned precast concrete beam–column connections." *Magazine of Concrete Research*, *73*(9). https://doi.org/10.1680/jmacr.19.00083, 2021.
[18] S. Paudel, G. Tanapornraweekit, S. Tangtermsirikul, "Numerical study on seismic performance improvement of composite wide beam-column interior joints," *Journal of Building Engineering*, *46*. https://doi.org/10.1016/j.jobe.2021.103637, 2022.
[19] G. Zhipeng, G. Haishan, L. Liming, S. Pengfei, L. Siyao, Z. Yunfeng, Z. Jian, "Nonlinear finite element analysis of post-tensioned precast prestressed slab-beam-column joints," *Structures*, *58*. https://doi.org/10.1016/j.istruc.2023.105438, 2023.
[20] Z. X. Li, H. Liu, Y. Shi, Y. Ding, "Numerical and analytical investigation on progressive collapse resistance of prestressed precast concrete frame structures," *Journal of Building Engineering*, 52. https://doi.org/10.1016/j.jobe.2022.104417, 2022.
[21] M. Khodaei, M. H. Saghafi, A. Golafshar, "Seismic retrofit of exterior beam-column joints using steel angles connected by PT bars," *Engineering Structures*, *236*. https://doi.org/10.1016/j.engstruct.2021.112111, 2021.
[22] A. Maddah, A. Golafshar, M. H Saghafi, "3D RC beam–column joints retrofitted by joint enlargement using steel angles and post-tensioned bolts," *Engineering Structures*, *220*. https://doi.org/10.1016/j.engstruct.2020.110975, 2020.
[23] (FEMA), F. E. M. A. Interim Protocols For Determining Seismic Performance Characteristics of Structural and Nonstructural Components Through Laboratory Testing. In *FEMA 461* (Issue June), 2007.
[24] J. B. Mander, M. J. N. Priestley, R. Park, "Theoretical stress-strain model for confined concrete," *Journal of Structural Engineering*, *114*(8), 1804–1826. https://doi.org/10.1061/(asce)0733-9445(1988)114:8(1804), 1988.
[25] E. Tuncer, C. Karageyik, E. Canbay, N. Muka, B. Binici, "Seismic performance of post-tensioned cast-in-place reinforced concrete structures based on component testing," *Journal of Building Engineering*, *122*. https://10.1016/j.jobe.2026.115744, 2026.